Geosci. Model Dev. Discuss., 7, 4251–4290, 2014
www.geosci-model-dev-discuss.net/7/4251/2014/
doi:10.5194/gmdd-7-4251-2014

Geoscientific Model Development Discussions
Open Access

A high-order conservative collocation scheme and its application to global shallow water equations

C. Chen[1], X. Li[2], X. Shen[2], and F. Xiao[3]

[1]School of Human Settlement and Civil Engineering, Xi'an Jiaotong University, Xi'an, China
[2]Center of Numerical Weather Prediction, China Meteorological Administration, Beijing, China
[3]Department of Energy Sciences, Tokyo Institute of Technology, Yokohama, Japan

Received: 31 May 2014 – Accepted: 10 June 2014 – Published: 10 July 2014

Correspondence to: C. Chen (cgchen@mail.xjtu.edu.cn, cgchen@imech.ac.cn)

Published by Copernicus Publications on behalf of the European Geosciences Union.

Abstract

An efficient and conservative collocation method is proposed and used to develop a global shallow water model in this paper. Being a nodal type high-order scheme, the present method solves the point-wise values of dependent variables as the unknowns within each control volume. The solution points are arranged as Gauss–Legendre points to achieve the high-order accuracy. The time evolution equations to update the unknowns are derived under the flux-reconstruction (FR) framework (Huynh, 2007). Constraint conditions used to build the spatial reconstruction for the flux function include the point-wise values of flux function at the solution points, which are computed directly from the dependent variables, as well as the numerical fluxes at the boundaries of the control volume which are obtained as the Riemann solutions between the adjacent cells. Given the reconstructed flux function, the time tendencies of the unknowns can be obtained directly from the governing equations of differential form. The resulting schemes have super convergence and rigorous numerical conservativeness.

A three-point scheme of fifth-order accuracy is presented and analyzed in this paper. The proposed scheme is adopted to develop the global shallow-water model on the cubed-sphere grid where the local high-order reconstruction is very beneficial for the data communications between adjacent patches. We have used the standard benchmark tests to verify the numerical model, which reveals its great potential as a candidate formulation for developing high-performance general circulation models.

1 Introduction

A recent trend in developing global models for atmospheric and oceanic general circulations is the increasing use of the high order schemes that make use of local reconstructions and have the so-called spectral convergence. Among many others are those reported in Giraldo et al. (2002); Thomas and Loft (2005); Giraldo and Warburton (2005); Nair et al. (2005a, b); Taylor and Fournier (2010); Blaise and St-Cyr (2012). Two

GMDD
7, 4251–4290, 2014

major advantages that make these models attractive are (1) they can reach the targeted numerical accuracy more quickly by increasing the number of degrees of freedom (or unknowns), and (2) they can be more computationally intensive with respect to the data communications in parallel processing (Dennis et al., 2012).

The discontinuous Galerkin (DG) (Cockburn et al., 2000; Hesthaven and Warburton, 2008) and spectral element (SE) (Patera, 1984; Karniadakis and Sherwin, 2005) methods are the widely used framework in this context. A more general formulation, so-called flux reconstruction (FR), was presented in Huynh (2007) which covers a wide spectrum of nodal type schemes, including the DG and SE as the special cases. An FR scheme solves the values at the solution points located within each grid element cell, and the cell integrated value, which are the weighted summation of the solutions, can be numerically conserved. We recently show in Xiao et al. (2013) that the flux reconstruction can be implemented in a more flexible way, and other new schemes can be generated by properly chosen different types of constraint conditions.

In this paper, we introduce a new scheme which is different from the existing nodal DG and SE methods under the FR framework. The scheme, so-called Gauss–Legendre-point based conservative collocation (GLPCC) method, is a kind of collocation method that solves the governing equations of differential form at the solution points, and is very simple and easy to follow. The Fourier analysis and numerical tests show that the present scheme has the super convergence property same as the DG method. A global shallow water equation (SWE) model has been developed by implementing the three-point GLPCC scheme on a cubed-sphere grid. The model has been verified by the benchmark tests. The numerical results show the fifth-order accuracy of the present global SWE model. All the numerical outputs look favourably comparable to other existing methods.

The rest of this paper is organized as follows. In Sect. 2, the numerical formulations in one dimensional case are described in detail. The extension of the proposed scheme to a global shallow water model on cubed-sphere grid is then discussed in Sect. 3. In Sect. 4, several widely used benchmark tests are solved by the proposed model to

GMDD
7, 4251–4290, 2014

verify its performance in comparison with other existing models. Finally, a short conclusion is given in Sect. 5.

2 Numerical formulations

2.1 Scheme in one dimensional scalar case

The first order scalar hyperbolic conservation law in one dimension is solved in this subsection,

$$\frac{\partial q}{\partial t} + \frac{\partial f(q)}{\partial x} = 0, \tag{1}$$

where q is dependent variable and f is flux function.

The computational domain, $x \in [x_l, x_r]$, is divided into I elements with the grid spacing of $\Delta x_i = x_{i+\frac{1}{2}} - x_{i-\frac{1}{2}}$ for the ith element C_i : $\left[x_{i-\frac{1}{2}}, x_{i+\frac{1}{2}}\right]$.

A class of schemes can be devised under the framework of the flux reconstruction (FR) (Huynh, 2007; Xiao et al., 2013). For each grid element, e.g. C_i, the point values, q_{im} ($m = 1, 2, \ldots, M$), defined at the solution points (x_{im}) which are located within the element, are treated as the computational variables (unknowns). High order schemes can be built by increasing the number of the solution points. In this paper, we describe the GLPCC scheme that has three solution points for each grid element ($M = 3$).

Three local degrees of freedom (DOFs) (unknowns), i.e. q_{im}, $m = 1$ to 3, are pointwisely defined at solution points x_{im} within each element as shown in Fig. 1 (hollow circles). To achieve the best accuracy, the DOFs are arranged at Gauss–Legendre points,

$$x_{i1} = x_i - \frac{1}{2}\sqrt{\frac{3}{5}}\Delta x_i,\ x_{i2} = x_i \text{ and } x_{i3} = x_i + \frac{1}{2}\sqrt{\frac{3}{5}}\Delta x_i, \tag{2}$$

where x_i is the center of the element $x_i = (x_{i-\frac{1}{2}} + x_{i+\frac{1}{2}})/2$.

GMDD
7, 4251–4290, 2014

The unknowns are updated by applying the differential-form governing equations Eq. (1) at solution points as

$$\frac{\partial q_{im}}{\partial t} = -\left[\frac{\partial f(q)}{\partial x}\right]_{im}. \tag{3}$$

As a result, the key task left is to evaluate the derivatives of the flux function, which is realized by reconstructing the piecewise flux function, $\mathcal{F}_i(x)$, over each element. Once the reconstructed flux function is obtained, the derivative of flux function is approximated by

$$\left[\frac{\partial f(q)}{\partial x}\right]_{im} \approx \left[\frac{\partial \mathcal{F}_i(x)}{\partial x}\right]_{im}. \tag{4}$$

In this study, we assume that the reconstructed flux function over the ith element, $\mathcal{F}_i(x)$, has the form of

$$\mathcal{F}_i(x) = c_i^0 + c_i^1(x - x_i) + c_i^2(x - x_i)^2 + c_i^3(x - x_i)^3 + c_i^4(x - x_i)^4, \tag{5}$$

where the coefficients, c_i^0, $c_i^1, \ldots,$ c_i^4, are determined by a collocation method, which meets five constrained conditions specified at five constrained points (shown in Fig. 1 by solid circles) as

$$\begin{cases} \mathcal{F}_i(x_{im}) & = f(q_{im}),\ m = 1 \text{ to } 3 \\ \mathcal{F}_i\left(x_{i-\frac{1}{2}}\right) & = \tilde{f}_{i-\frac{1}{2}} \\ \mathcal{F}_i\left(x_{i+\frac{1}{2}}\right) & = \tilde{f}_{i+\frac{1}{2}} \end{cases} \tag{6}$$

where $\tilde{f}_{i\pm\frac{1}{2}}$ are the values of flux function at the interfaces between different elements.

In Eq. (6), $f(q_{im})$ are calculated by three known DOFs at solution points. The values of flux function at interfaces are obtained by solving the Riemann problems with the values of dependent variables at the interfaces between two neighboring elements, which

GMDD
7, 4251–4290, 2014

are interpolated separately from two adjacent elements. Considering the interface at $x_{i-\frac{1}{2}}$, we get two values of flux function from elements C_{i-1} and C_i as

$$f^L_{i-\frac{1}{2}} = f\left(q^L_{i-\frac{1}{2}}\right) = f\left[Q_{i-1}\left(x_{i-\frac{1}{2}}\right)\right] \quad \text{and} \quad f^R_{i-\frac{1}{2}} = f\left(q^R_{i-\frac{1}{2}}\right) = f\left[Q_i\left(x_{i-\frac{1}{2}}\right)\right], \tag{7}$$

where $Q_i(x)$ is a spatial reconstruction for dependent variable based on local DOFs, having the form of

$$Q_i(x) = \sum_{m=1}^{3} [\mathcal{L}_m(x) q_{im}], \tag{8}$$

where the Lagrange basis function $\mathcal{L}_m(x) = \prod_{s=1, s\neq m}^{3} \frac{x - x_{\text{is}}}{x_{im} - x_{\text{is}}}$.

Then the numerical flux $\tilde{f}_{i-\frac{1}{2}}$ at the element interface is obtained by an approximate Riemann solver as,

$$\tilde{f}_{i-\frac{1}{2}} = \frac{1}{2}\left[f^L_{i-\frac{1}{2}} + f^R_{i-\frac{1}{2}}\right] + \frac{1}{2} a \left[q^L_{i-\frac{1}{2}} - q^R_{i-\frac{1}{2}}\right], \tag{9}$$

where $a = \left|f'\left(q^{\text{avg}}_{i-\frac{1}{2}}\right)\right|$ with $f'(q) = \frac{\partial f(q)}{\partial q}$ being the characteristic speed. A simple averaging $q^{\text{avg}}_{i-\frac{1}{2}} = \frac{q^L_{i-\frac{1}{2}} + q^R_{i-\frac{1}{2}}}{2}$ is used in the present paper.

It is easy to show that the proposed scheme is conservative in terms of the volume-integrated average of each element,

$$\overline{q}_i = \sum_{m=1}^{3} (w_{im} q_{im}), \tag{10}$$

GMDD
7, 4251–4290, 2014

where the weights w_{im} are obtained by integrating the Lagrange basis function as

$$w_{im} = \frac{1}{\Delta x_i} \int_{x_{i-\frac{1}{2}}}^{x_{i+\frac{1}{2}}} \mathcal{L}_m(x)\mathrm{d}x. \tag{11}$$

A direct proof of this observation is obtained by integrating Eq. (3) over the grid element, yielding the following conservative formulation,

$$\frac{\mathrm{d}\overline{q}_i}{\mathrm{d}t} = \sum_{m=1}^{3} \left(w_{im} \frac{\mathrm{d}q_{im}}{\mathrm{d}t} \right) = -\frac{1}{\Delta x} \left(\tilde{f}_{i+\frac{1}{2}} - \tilde{f}_{i-\frac{1}{2}} \right). \tag{12}$$

With the above spatial discretization, Runge–Kutta method is used to solve the following semi-discrete equation,

$$\frac{\mathrm{d}q_{im}}{\mathrm{d}t} = \mathcal{D}(q^\star), \tag{13}$$

where $\mathcal{D}$ represents the spatial discretisation and $q^\star$ is the dependent variables known at time $t = t^\star$.

A fifth-order Runge–Kutta scheme is adopted in the numerical tests to examine the convergence rate,

$$q_{im}(t^\star + \Delta t) = q^\star_{\mathrm{ip}} + \Delta t \left(\frac{17}{144} d_1 + \frac{25}{36} d_3 + \frac{1}{72} d_4 - \frac{25}{72} d_5 + \frac{25}{48} d_6 \right), \tag{14}$$

GMDD
7, 4251–4290, 2014

where

$$\begin{cases} d_1 &= \mathcal{D}\left(q^*\right) \\ d_2 &= \mathcal{D}\left(q^* + \frac{1}{5}\Delta t d_1\right) \\ d_3 &= \mathcal{D}\left(q^* + \frac{2}{5}\Delta t d_2\right) \\ d_4 &= \mathcal{D}\left(q^* + \frac{9}{4}\Delta t d_1 + \frac{15}{4}\Delta t d_2 - 5\Delta t d_3\right) \\ d_5 &= \mathcal{D}\left(q^* - \frac{63}{100}\Delta t d_1 + \frac{9}{5}\Delta t d_2 - \frac{13}{20}\Delta t d_3 + \frac{2}{25}\Delta t d_4\right) \\ d_6 &= \mathcal{D}\left(q^* - \frac{6}{25}\Delta t d_1 + \frac{4}{5}\Delta t d_2 + \frac{2}{15}\Delta t d_3 + \frac{8}{75}\Delta t d_4\right) \end{cases} \tag{15}$$

In other cases, a third-order scheme is adopted to reduce the computational cost, which does not noticeably degrade the numerical accuracy since the truncation errors of the spatial discretisation are usually dominant. It is written as

$$q_{im}(t^* + \Delta t) = q^*_{\mathrm{ip}} + \Delta t \left(\frac{1}{6}d_1 + \frac{1}{6}d_2 + \frac{2}{3}d_3\right), \tag{16}$$

where

$$\begin{cases} d_1 = & \mathcal{D}\left(q^*\right) \\ d_2 = & \mathcal{D}\left(q^* + \Delta t d_1\right) \\ d_3 = & \mathcal{D}\left(q^* + \frac{1}{4}\Delta t d_1 + \frac{1}{4}\Delta t d_2\right) \end{cases}. \tag{17}$$

2.2 Spectral analysis and convergence test

We conduct the spectral analysis (Huynh, 2007; Xiao et al., 2013) to theoretically study the performance of GLPCC scheme by considering the following linear equation

$$\frac{\partial q}{\partial t} + c\frac{\partial q}{\partial x} = 0 \ (x \in [-\infty, +\infty]) \text{ and } c = 1. \tag{18}$$

The linear equation is discretised on a uniform grid with $\Delta x = 1$. Since $c > 0$, the spatial discretisation for the three DOFs defined in element C_i involves the six DOFs

GMDD
7, 4251–4290, 2014

within elements C_i and C_{i-1}. Using the proposed scheme, we have the semi-discrete equation as

$$\frac{d}{dt}\begin{bmatrix} q_{i1} \\ q_{i2} \\ q_{i3} \end{bmatrix} = \begin{bmatrix} c_{i-1,11} & c_{i-1,12} & c_{i-1,13} & c_{i,11} & c_{i,12} & c_{i,13} \\ c_{i-1,21} & c_{i-1,22} & c_{i-1,23} & c_{i,21} & c_{i,22} & c_{i,23} \\ c_{i-1,31} & c_{i-1,32} & c_{i-1,33} & c_{i,31} & c_{i,32} & c_{i,33} \end{bmatrix} \begin{bmatrix} q_{i-1,1} \\ q_{i-1,2} \\ q_{i-1,3} \\ q_{i1} \\ q_{i2} \\ q_{i3} \end{bmatrix}. \tag{19}$$

With a wave solution $q(x,t) = e^{I\omega(x+t)}$, semi-discrete formulation Eq. (19) is written as

$$\frac{\mathrm{d}\boldsymbol{q}_i}{\mathrm{d}t} = \mathcal{P}\boldsymbol{q}_i, \tag{20}$$

where $\boldsymbol{q}_i = [q_{i1}, q_{i2}, q_{i3}]^T$ and

$$\mathcal{P} = \begin{bmatrix} c_{i-1,11}e^{-I\omega} + c_{i,11} & c_{i-1,12}e^{-I\omega} + c_{i,12} & c_{i-1,13}e^{-I\omega} + c_{i,13} \\ c_{i-1,21}e^{-I\omega} + c_{i,21} & c_{i-1,22}e^{-I\omega} + c_{i,22} & c_{i-1,23}e^{-I\omega} + c_{i,23} \\ c_{i-1,31}e^{-I\omega} + c_{i,31} & c_{i-1,32}e^{-I\omega} + c_{i,32} & c_{i-1,33}e^{-I\omega} + c_{i,33} \end{bmatrix}. \tag{21}$$

The exact solution to Eq. (18) is

$$\frac{\mathrm{d}q}{\mathrm{d}t} = -I\omega q. \tag{22}$$

The numerical property of the proposed scheme can be examined by analysing the eigenvalues of matrix $\mathcal{P}$ in Eq. (21). Truncation errors of spatial discretization are computed by comparing the principal eigenvalues of matrix $\mathcal{P}$ and the exact solution $-I\omega$ and the convergence rate can be approximately estimated by errors for two different

GMDD
7, 4251–4290, 2014

wavenumbers. The results are shown in Table 1 and fifth-order accuracy is achieved. The spectrum of the eigen matrix of Eq. (21) is shown in Fig. 2. A scheme achieves better numerical performance when the hollow circles become closer to imaginary axis. And the maximum of spectral radius determines the largest available CFL number, i.e. larger spectral radius corresponding to smaller available CFL number. Numerical dispersion and dissipation relations dominated by the principal eigenvalues are shown in Fig. 3. Numerical properties of several schemes were analyzed in Xiao et al. (2013), shown in their Fig. 1 for spectra and Fig. 2 for numerical dispassion and dispersion relations. The proposed scheme has the similar numerical properties as DG3 (Huynh, 2007) and MCV5 (li and Xiao, 2009) schemes. Compared with DG3 scheme, the proposed scheme is easier to be implemented and thus has less computational overheads. Though MCV5 scheme gives better spectra (eigenvalues are closer to imaginary) than DG3 scheme and the present scheme, it adopts more local DOFs under the same grid spacing, i.e. $4I+1$ DOFs for MCV5 and $3I$ DOFs for DG3 and the present scheme where I is the total number of elements. Both MCV5 and the present scheme are accelerating up to wavenumber 2π. Considering the results of spectral analysis, the proposed scheme is a very competitive framework to build high-order schemes compared with existing advanced methods.

Advection of a smooth sine wave is then computed by GLPCC scheme on a series refined uniform grids to numerically checking the converge rate. The test case is specified by solving Eq. (18) with initial condition $q(x,0) = \sin(2\pi x)$ and periodical boundary condition over $x \in [0,1]$.

CFL number of 0.1 is adopted in this example. Normalized l_1, l_2 and l_∞ and corresponding convergence rate are given in Table 2. Again, the fifth-order convergence is obtained, which agrees with the conclusion in the above spectral analysis.

GMDD
7, 4251–4290, 2014

2.3 Extension to system equations

The proposed scheme is then extended to a hyperbolic system with L equations in one dimension, which is written as

$$\frac{\partial \boldsymbol{q}}{\partial t} + \frac{\partial \boldsymbol{f}(\boldsymbol{q})}{\partial x} = 0, \tag{23}$$

where $\boldsymbol{q}$ is the vector of dependent variables and $\boldsymbol{f}$ the vector of flux functions.

Above formulations can be directly applied to each equation of the hyperbolic system, except that the Riemann problem, which is required at interfaces between different elements to determine the values of flux functions, is solved for a coupled system of equations.

For a hyperbolic system of equations, the approximate Riemann solver used at interface $x_{i-\frac{1}{2}}$ is obtained by rewriting Eq. (9) as

$$\boldsymbol{f}_{i-\frac{1}{2}} = \frac{1}{2}\left[\boldsymbol{f}^L_{i-\frac{1}{2}} + \boldsymbol{f}^R_{i-\frac{1}{2}}\right] + \frac{1}{2}\mathbf{a}\left[\boldsymbol{q}^L_{i-\frac{1}{2}} - \boldsymbol{q}^R_{i-\frac{1}{2}}\right], \tag{24}$$

where the vectors $\boldsymbol{f}^L_{i-\frac{1}{2}}$, $\boldsymbol{f}^R_{i-\frac{1}{2}}$, $\boldsymbol{q}^L_{i-\frac{1}{2}}$ and $\boldsymbol{q}^R_{i-\frac{1}{2}}$ are evaluated by applying the formulations designed for scalar case to each component of the vector. In this paper, we use a simple approximate Riemann solver, the local Lax–Friedrich (LLF) solver, where $\mathbf{a}$ is reduced to a positive real number as

$$\mathbf{a} = \max\left(|\lambda_1|, |\lambda_2|, \ldots, |\lambda_L|\right), \tag{25}$$

where λ_l ($l = 1$ to L) are eigenvalues of matrix $\mathbf{A}\left(\boldsymbol{q}^{\text{avg}}_{i-\frac{1}{2}}\right)$ with $\mathbf{A}(\boldsymbol{q}) = \frac{\partial \boldsymbol{f}(\boldsymbol{q})}{\partial \boldsymbol{q}}$ and $\boldsymbol{q}^{\text{avg}}_{i-\frac{1}{2}} = \frac{\boldsymbol{q}^L_{i-\frac{1}{2}} + \boldsymbol{q}^R_{i-\frac{1}{2}}}{2}$.

GMDD
7, 4251–4290, 2014

3 Global shallow-water model on cubed-sphere grid

3.1 Cubed-sphere grid

The cubed-sphere grid (Sadourny, 1972), shown in Fig. 4, is obtained by projecting an inscribed cube onto a sphere. As a result, the surface of a sphere is divided into six identical patches and six identical curvilinear coordinates are then constructed. Two kinds of projections are adopted to construct the local curvilinear coordinates, i.e. gnomonic and conformal projections (Rancic et al., 1996). Considering the analytic projection relations and more uniform areas of the computational elements, the equiangular gnomonic projection is adopted in the present study. The transformation laws and the projection relations can be referred to Nair et al. (2005a, b) for details. Whereas, a side-effect of this selection is that the discontinuous coordinates are found along the boundary edges between adjacent patches. In Chen and Xiao (2008), we have shown that the compact stencils for the spatial reconstructions through using local DOFs are beneficial to suppress the extra numerical errors due to the discontinuous coordinates.

3.2 Global shallow-water model

The local curvilinear coordinate system (ξ, η) are shown in Fig. 5, where P is a point on sphere surface, and P' is corresponding point on the cube surface through a gnomonic projection. λ and θ represent the longitude and latitude. α and β are central angles spanning from $-\frac{\pi}{4}$ to $\frac{\pi}{4}$ for each patch. Local coordinates are defined by $\xi = R\alpha$ and $\eta = R\beta$ where R is the radius of the Earth.

To build a high-order global model, the governing equations is rewritten onto the general curvilinear coordinates. As a result, the numerical schemes developed for Cartesian grid are straightforwardly applied in the computational space. The shallow-water equations are recast on each spherical patch in flux form as

$$\frac{\partial \boldsymbol{q}}{\partial t} + \frac{\partial \boldsymbol{e}(\boldsymbol{q})}{\partial \xi} + \frac{\partial \boldsymbol{f}(\boldsymbol{q})}{\partial \eta} = \mathbf{s}(\boldsymbol{q}), \tag{26}$$

GMDD
7, 4251–4290, 2014

where dependent variables are $\boldsymbol{q} = \left[\sqrt{G}h,\ u,\ v\right]^T$ with water depth h, covariant velocity vector (u,v) and Jacobian of transformation $\sqrt{G}$, flux vectors are $\boldsymbol{e} = \left[\sqrt{G}h\tilde{u},\ g(h+h_s)+\frac{1}{2}(\tilde{u}u+\tilde{v}v),\ 0\right]^T$ in ξ direction and $\boldsymbol{f} = \left[\sqrt{G}h\tilde{v},\ 0, g(h+h_s)+\frac{1}{2}(\tilde{u}u+\tilde{v}v)\right]^T$ in η direction with gravitational acceleration g, height of the bottom mountain h_s and contravariant velocity vector $(\tilde{u},\tilde{v})$, source term is $\mathbf{s} = \left[0,\ \sqrt{G}\tilde{v}(f+\zeta),\ -\sqrt{G}\tilde{u}(f+\zeta)\right]^T$ with Coriolis parameter $f = 2\Omega\sin\theta$, rotation speed of the Earth $\Omega = 7.292\times10^{-5}s^{-1}$ and relative vorticity $\zeta = \frac{1}{\sqrt{G}}\left(\frac{\partial v}{\partial\xi}-\frac{\partial u}{\partial\eta}\right)$. The expression of metric tensor can be found in Chen and Xiao (2008).

Here, taking $\sqrt{G}h$ as the model variable assures the global conservation of total mass. And the total height is used in the flux term. Consequently, the proposed model can easily deal with the topographic source term in a conservative way (Xing and Shu, 2005).

The numerical formulations for two dimensional schemes are easily obtained under the present framework by implementing the one-dimensional GLPCC formulations in ξ and η directions respectively as

$$\left(\frac{\partial \boldsymbol{q}}{\partial t}\right) = \left(\frac{\partial \boldsymbol{q}}{\partial t}\right)^{\xi} + \left(\frac{\partial \boldsymbol{q}}{\partial t}\right)^{\eta} + \mathbf{s}, \tag{27}$$

where

$$\left(\frac{\partial \boldsymbol{q}}{\partial t}\right)^{\xi} = -\frac{\partial \boldsymbol{e}(\boldsymbol{q})}{\partial \xi} \text{ and } \left(\frac{\partial \boldsymbol{q}}{\partial t}\right)^{\eta} = -\frac{\partial \boldsymbol{f}(\boldsymbol{q})}{\partial \eta} \tag{28}$$

are discretised along the grid lines in ξ and η directions.

We describe the numerical procedure in ξ direction here as follows. In η direction, similar procedure is adopted for spatial discretisation by simply exchanging e and ξ

GMDD
7, 4251–4290, 2014

with f and η. Considering three DOFs, i.e. $\boldsymbol{q}_{ij1nk}$, $\boldsymbol{q}_{ij2nk}$ and $\boldsymbol{q}_{ij3nk}$, along the nth row (n = 1 to 3) of element $C_{ijk} = \left[\xi_{i-\frac{1}{2}}, \xi_{i+\frac{1}{2}}\right] \times \left[\eta_{j-\frac{1}{2}}, \eta_{j+\frac{1}{2}}\right]$ on patch k (defined at solution points denoted by the hollow circles in Fig. 6), we have the task to solve the following equations

$$\left(\frac{\partial \boldsymbol{q}_{ijmnk}}{\partial t}\right)^{\xi} = -\left(\frac{\partial \boldsymbol{e}}{\partial \xi}\right)_{ijmnk}. \tag{29}$$

As in one dimensional case, a fourth-order polynomial $\mathcal{E}_{ijnk}(x)$ is built for spatial reconstructions of flux functions $\boldsymbol{e}$ to calculate the derivative of $\boldsymbol{e}$ with regard to ξ as

$$\left(\frac{\partial \boldsymbol{e}}{\partial \xi}\right)_{ijmnk} = \left[\frac{\partial \mathcal{E}_{ijnk}(\xi)}{\partial \xi}\right]_{ijmnk}, \tag{30}$$

where $\mathcal{E}(\xi)$ can be obtained by applying the constrained conditions at five constrained points (solid circles in Fig. 6) along the nth row of element C_{ijk}, which are point-wise values of flux functions $\boldsymbol{e}$ including three from DOFs directly and other two by solving Riemann problems along the nth lines of different elements.

The LLF approximate Riemann solver is adopted. It means that the parameter $\mathbf{a}$ in Eq. (24) reads $\mathbf{a} = |\tilde{u}| + \sqrt{G^{11}gh}$. Details of solving Riemann problem in global shallow-water model using governing equations Eq. (26) can be referred to Nair et al. (2005b).

How to set up the boundary conditions along twelve patch boundary is a key problem to construct a global model on cubed-sphere grid. With the enough information from the adjacent patch, above numerical formulations can be applied on each patch independently. In present study, the values of dependent variables are required to be interpolated from the grid lines in the adjacent patch, for example, as shown in Fig. 7 for boundary edge between patch 1 and patch 4. When we solving the Riemann problem at point P on patch 1, $\boldsymbol{q}_P^R = \left[\left(\sqrt{G}h\right)_P^R, u_p^R, v_P^R\right]^T$ is obtained by interpolation along

GMDD
7, 4251–4290, 2014

the grid line $\overline{PP_1}$. Whereas, $\boldsymbol{q}_P^L = \left[\left(\sqrt{G}h\right)_P^L, u_p^L, v_P^L\right]^T$ need to be interpolated from the DOFs defined along grid line $\overline{P_4P}$ on patch 4. Since the coordinates on patch 1 and patch 4 is discontinuous at point P, the values of the covariant velocity vector on the coordinate system on patch 4 should be projected to coordinate system on patch 1 and the values of the scalar can be adopted directly. Different from our previous study (Chen and Xiao, 2008), we solve the Riemann problem at patch boundary only in the direction perpendicular to the edge in present study. The parameter **a** in Eq. (24) is determined by the contravariant velocity component and the water depth, which are exactly same on two adjacent patches. As a result, solving Riemann problem obtains the same result wherever the numerical procedure is conducted on patch 1 or patch 4. So, no additional corrections are required and the global conservation is guaranteed automatically.

4 Numerical tests

Representative benchmark tests, three from Williamson's standard test set (Williamson et al., 1992) and one introduced in Galewsky et al. (2004), are checked in this section to verify the performance of the proposed global shallow-water model. All measurements of errors are defined following Williamson et al. (1992).

4.1 Williamson's standard case 2: steady-state geostrophic flow

A balanced initial condition is specified in case by using a height field as

$$gh = gh_0 - \left(R\Omega u_0 + \frac{u_0^2}{2}\right)(-\cos\lambda\cos\theta\sin\gamma + \sin\theta\cos\gamma)^2 \tag{31}$$

GMDD
7, 4251–4290, 2014

where $gh_0 = 2.94 \times 10^4$, $u_0 = 2\pi R/(12\,\text{days})$ and the parameter γ represents the angle between the rotation axis and polar axis of the Earth, and a velocity field (velocity components in latitude/longitude grid u_λ and u_θ) as

$$\begin{cases} u_\lambda &= u_0(\cos\theta\cos\gamma + \sin\theta\cos\lambda\sin\gamma) \\ u_\theta &= -u_0\sin\lambda\sin\gamma \end{cases}. \tag{32}$$

As a result, both height and velocity fields should keep unchanging during integration. Additionally, the height field in this test case is considerably smooth. Thus we run this test on a series of refined grids to check the convergence rate of GLPCC global model. The results of l_1, l_2 and l_∞ errors and convergence rates are in Table 3. After extending the proposed high-order scheme to the spheric geometry through the application of the cubed-sphere grid, the original fifth-order accuracy as shown in one-dimensional simulations and spectral analysis preserved in this test. Numerical results of height fields and absolute errors are shown in Fig. 8 for test on grid G_{12}, which means there are 12 elements in both ξ and η directions on every patch, in different flow directions. i.e. $\gamma = 0$ and $\gamma = \frac{\pi}{4}$. Compared with our former global model on cubed sphere, the present model is more accurate in this test. On grid G_{20} (240 DOFs along the equator), the normalized errors are $l_1 = 1.278 \times 10^{-7}$, $l_2 = 2.008 \times 10^{-7}$ and $l_\infty = 8.045 \times 10^{-7}$, which are almost one order smaller than those on grid $32 \times 32 \times 6$ (with similar number of DOFs, 256 DOFs along the equator) in Chen and Xiao (2008). The influence of patch boundaries on the numerical results can be found in the plots of the absolute errors. The distributions of absolute errors can reflect the locations of patch boundaries, especially in the flow with $\gamma = 0$.

GMDD
7, 4251–4290, 2014

4.2 Williamson's standard case 5: zonal flow over an isolated mountain

The total height and velocity field in case is same as above case 2 with $\gamma = 0$, except $h_0 = 5960\,\mathrm{m}$ and $u_0 = 20\,\mathrm{m\,s^{-1}}$. A bottom mountain is specified as

$$h_s = h_{s0}\left(1 - \frac{r}{r_0}\right), \tag{33}$$

where $h_{s0} = 2000\,\mathrm{m}$, $r_0 = \frac{\pi}{9}$ and $r = \min\left[r_0, \sqrt{(\lambda - \lambda_c)^2 + (\theta - \theta_c)^2}\right]$.

This test is adopted to check the performance of a shallow-water model to deal with a topographic source term. We run this test on a series of refined grid G_6, G_{12}, G_{24} and G_{48}. Numerical results of height fields are shown in Fig. 9 for total height field of the test on grid G_{12} at day 5, 10 and 15, which agree well with the spectral transform solutions on T213 grid (Jakob-Chien et al., 1995). Furthermore, the oscillations occurring at boundary of bottom mountain observed in spectral transform solutions are completely removed through the conservative treatment of topographic source term. The numerical results on finer grids are not depicted here since they are visibly identical to results shown in Fig. 9. Present model assures the rigorous conservation of the total mass. The conservation errors of total energy and enstrophy are interest for atmospheric modelling. As shown in Fig. 10, the conservation errors for total energy (left panel) and potential enstrophy (right panel) of tests on a series of refined grid are checked. As above case, to compare with our former fourth-order model this test case is checked on grid G_{20} having the similar DOFs on former $32 \times 32 \times 6$ grid. The conservation errors are -9.288×10^{-7} for total energy and -1.388×10^{-5} for potential enstrophy and much smaller than those by fourth-order model in Chen and Xiao (2008).

4.3 Williamson's standard case 6: Rossy–Haurwitz wave

Rossby–Haurwitz wave case checks a flow field including the phenomena of a large range of scales. As a result, the high-order schemes are always preferred to better

GMDD
7, 4251–4290, 2014

capture the evolution of small scales. The spectral transform solution on fine T213 grid given by Jakob-Chien et al. (1995) is wildly accepted as the reference solution to this test due to the good capability of spectral method to reproduce the behaviour of small scales. Numerical results of height fields by GLPCC model are shown in Fig. 11 for tests on grids G_{12} and G_{24} at day 7 and 14. At day 7, no visible difference is observed between the solutions on different grids and both agree well with the reference solution. At day 14, obvious differences are found on different grids. Eight circles of 8500 m exist in the result on coarser grid G_{12}, which are also found in the spectral transform solution on T42 grid, but not in the results on finer grid G_{24} by GLPCC model and the spectral transform ones on T63 and T213 grids. Additionally, the contour lines of 8100 m exists in spectral transform solution on T213 grid, but not in present results and spectral transform ones on T42 and T63 grids. According to the analysis in Thuburn and Li (2000), this is due to the less inherent numerical viscosity on finer grid. As in case 5, conservation errors for total energy and potential enstrophy in Rossby–Haurwitz test are also shown in Fig. 12 for tests with different resolutions. Total energy error of -6.131×10^{-6} and potential enstrophy error -1.032×10^{-3} are obtained by the present model running on grid G_{20}, which are smaller than those by our fourth-order model on $32 \times 32 \times 6$ grid (Chen and Xiao, 2008). This test was also checked in Chen et al. (2014) by a third-order model (see their Fig. 19c and d), where much more DOFs (nine times than those on grid G_{24}) are adopted to obtain a results without eight circles of 8500 m. High-order accuracy is very beneficial to simulating this test and the atmospheric dynamics.

4.4 Barotropic instability

A barotropic instability test was proposed in Galewsky et al. (2004). Two kinds of setup of this test are usually checked in literatures, i.e. the balanced setup and unbalanced setup. The balanced setup is same as Williamson's standard case 2, except the water depth changes with much larger gradient within a very narrow belt zone. This test is of special interest for global models on the cubed-sphere grid, since that narrow belt zone is located along the boundary edges between patch 5 and patches 1, 2, 3, and 4.

GMDD
7, 4251–4290, 2014

Extra numerical errors near boundary edges would easily pollute the numerical results. In practice, 4-wave pattern errors may dominate the simulations on coarse grids. For this case, we run the proposed model on a series of refined grids. By checking the convergence of the numerical results, we can figure out if the extra numerical errors generated by discontinuous coordinates can be suppressed by the proposed models with the increase of the resolution. The unbalanced setup introduces a small perturbation to the height field. Thus, the balanced condition can not be preserved and the flow will evolve to a very complex pattern. Exact solution does not exist for unbalanced setup and a spectral transform solution on T341 grid to this case given in Galewsky et al. (2004) at day 6 is widely adopted as reference solution. The details of setup of this test can be referred to Galewsky et al. (2004).

4.4.1 Balanced setup

We test the balanced setup at first. The proposed model runs on two grids with different resolutions of G_{24} and G_{72}. Numerical results of water depth after integrating for 5 days are shown in Fig. 13 and evolution of normalized l_1 errors of water depth of two simulations are depicted in Fig. 14. On a coarse grid with G_{24}, the numerical result is dominated by four-wave pattern errors and the balanced condition can not be preserved in simulation. The accuracy is obviously improved by increasing the resolution using grid G_{72}. The numerical result of height field at day 5 is visually identical to the initial condition. The improvement of the accuracy can be also proven by checking the velocity component u_θ. Numerical results of u_θ, which keeps zero in exact solution, vary within $\pm 31\,\mathrm{m\,s^{-1}}$ on grid G_{24} and much smaller range of $\pm 0.8\,\mathrm{m\,s^{-1}}$ on grid G_{72}. This test is more challenging for cubed-sphere grid than other quasi-uniform grids, e.g. Yin–Yang grid and icosahedral grid. As shown in Fig. 14, at very beginning of the simulation the l_1 errors increase to a magnitude of about 10^{-4} and this character does not change with the grid resolution. This evolution pattern of l_1 errors are different from those of models on Yin–Yang and icosahedral grids, where initial startup errors also decrease on fine grids as shown in Chen et al. (2014, Fig. 23).

GMDD
7, 4251–4290, 2014

4.4.2 Unbalanced setup

We run the unbalanced setup on a series of refined grids to check if the numerical result will converge to the reference solution on fine grid. Numerical results for relative vorticity field after integrating the proposed model for 6 days are shown in Fig. 15. Shown are results on four grids with gradually refined resolutions of G_{24}, G_{48}, G_{72} and G_{96}. On grid G_{24}, the structure of numerical results is very different from the reference solution. After refining the grid resolution, the result is improved on grid G_{48}. Except the structure in top-left conner, it looks very similar to the reference solution. On grid G_{72} and G_{96}, numerical results agree with reference solution very well and there is no obvious difference between these two contour plots. Compared with the results of our former fourth-order model, the contour lines look slightly less smooth. Similar results are found in the spectral transform reference solution. Since this test contains more significant gradients in the solution, a high-order scheme might need some extra numerical dissipation to remove the noise around the large-gradients. Increasing the grid solution can effectively reduce the magnitude of the oscillations as shown in the present simulation.

5 Conclusions

In this paper, a three-point high-order GLPCC scheme is proposed under the framework of flux reconstruction. Three local DOFs are defined within each element at Gauss–Legendre points and a super convergence of fifth order is achieved. This single-cell based method shares the advantages with the DG and SE methods, such as high-order accuracy, grid flexibility, global conservation and high scalability for parallel processing. Meanwhile, it is much simpler and easier to implement. With the application of the cubed-sphere grid, the global shallow water model has been constructed using GLPCC scheme. Benchmark tests are checked by using the present model, and

GMDD
7, 4251–4290, 2014

promising results reveal that it is a potential framework to develop high-performance general circulation models for atmospheric and oceanic dynamics.

Acknowledgements. This study is supported by the National Key Technology R&D Program of China (Grant 2012BAC22B01), the National Natural Science Foundation of China (Grants 11372242 and 41375108).

References

Blaise, S. and St-Cyr, A.: A dynamic hp-adaptive discontinuous Galerkin method for shallow water flows on the sphere with application to a global tsunami simulation, Mon. Weather Rev., 140, 978–996, 2012. 4252

Chen, C. G. and Xiao, F.: Shallow water model on cubed-sphere by multi-moment finite volume method, J. Comput. Phys., 227, 5019–5044, 2008. 4262, 4263, 4265, 4266, 4267, 4268

Chen, C. G., Li, X. L., Shen, X. S., and Xiao, F.: Global shallow water models based on multi-moment constrained finite volume method and three quasi-uniform spherical grids, J. Comput. Phys., 271, 191–223, 2014. 4268, 4269

Cockburn, B., Karniadakis, G., and Shu, C. (Eds.): Discontinuous Galerkin Methods: Theory, Computation and Applications, Vol. 11 of Lecture Notes Lecture Notes in Computational Science and Engineering, Springer, 1st Edn., 2000. 4253

Dennis, J., Edwards, J., Evans, K., Guba, O., Lauritzen, P., Mirin, A., St-Cyr, A., Taylor, M., and Worley, P.: CAM-SE: a scalable spectral element dynamical core for the community atmosphere model, Int. J. High Perform. C., 26, 74–89, 2012. 4253

Galewsky, J., Scott, R. K., and Polvani, L. M.: An initial-value problem for testing numerical models of the global shallow-water equations, Tellus, 56, 429–440, 2004. 4265, 4268, 4269

Giraldo, F. X. and Warburton, T.: A nodal triangle-based spectral element method for the shallow water equations on the sphere, J. Comput. Phys., 207, 129–150, 2005. 4252

Giraldo, F. X., Hesthaven, J. S., and Warburton, T.: Nodal high-order discontinuous Galerkin methods for the spherical shallow water equations, J. Comput. Phys., 181, 499–525, 2002. 4252

Hesthaven, J. and Warburton, T.: Nodal Discontinuous Galerkin Methods: Algorithms, Analysis, and Applications, Springer, 2008. 4253

GMDD

7, 4251–4290, 2014

Huynh, H. T.: A flux reconstruction approach to high-order schemes including discontinuous Galerkin methods 2007-4079, 2007, AIAA Paper, 2007. 4252, 4253, 4254, 4258, 4260
Ii, S. and Xiao, F.: High order multi-moment constrained finite volume method. Part I: Basic formulation, J. Comput. Phys., 228, 3669–3707, 2009. 4260
Jakob-Chien, R., Hack, J. J., and Williamson, D. L.: Spectral transform solutions to the shallow water test set, J. Comput. Phys., 119, 164–187, 1995. 4267, 4268
Karniadakis, G. and Sherwin, S.: Spectral/HP Element Methods for Computational Fluid Dynamics, Oxford University Press, 2005. 4253
Nair, R. D., Thomas, S. J., and Loft, R. D.: A discontinuous Galerkin transport scheme on the cubed sphere, Mon. Weather Rev., 133, 827–841, 2005a. 4252, 4262
Nair, R. D., Thomas, S. J., and Loft, R. D.: A discontinuous Galerkin global shallow water model, Mon. Weather Rev., 133, 876–887, 2005b. 4252, 4262, 4264
Patera, A.: A spectral element method for fluid dynamics: Laminar flow in a channel expansion, J. Comput. Phys., 54, 468–488, 1984. 4253
Rancic, M., Purser, R. J., and Mesinger, F.: A global shallow-water model using an expanded spherical cube: gnomonic versus conformal coordinates, Q. J. Roy. Meteorol. Soc., 122, 959–982, 1996. 4262
Sadourny, R.: Conservative finite-difference approximations of the primitive equations on quasi-uniform spherical grids, Mon. Weather Rev., 100, 136–144, 1972. 4262
Taylor, M. A. and Fournier, A.: A compatible and conservative spectral element method on unstructured grids, J. Comput. Phys., 229, 5879–5895, 2010. 4252
Thomas, S. and Loft, R.: The NCAR spectral element climate dynamical core: semi-implicit Eulerian formulation, J. Sci. Comput., 25, 307–322, 2005. 4252
Thuburn, J. and Li, Y.: Numericial simulations of Rossby-Haurwitz waves, Tellus A, 52, 181–189, 2000. 4268
Williamson, D. L., Drake, J. B., Hack, J. J., Jakob, R., and Swarztrauber, P. N.: A standard test set for numerical approximations to the shallow water equations in spherical geometry, J. Comput. Phys., 102, 211–224, 1992. 4265
Xiao, F., Ii, S., Chen, C., and Li, X.: A note on the general multi-moment constrained flux reconstruction formulation for high order schemes, Appl. Math. Model., 37, 5092–5108, 2013. 4253, 4254, 4258, 4260
Xing, Y. and Shu, C.-W.: High order finite difference WENO schemes with the exact conservation property for the shallow water equations, J. Comput. Phys., 208, 206–227, 2005. 4263

GMDD
7, 4251–4290, 2014

Table 1. Numerical errors at two wavenumbers and corresponding convergence rate.

Wavenumber	$\omega = \frac{\pi}{8}$	$\omega = \frac{\pi}{4}$	Order
Error	$-3.1408 \times 10^{-5} - 4.2715 \times 10^{-6} i$	$-5.0466 \times 10^{-7} - 3.4068 \times 10^{-8} i$	4.97

GMDD
7, 4251–4290, 2014

Table 2. Numerical errors and convergence rates for advection of a sine wave.

Resolution	l_1 error	order	l_2 error	Order	l_∞ error	Order
$I = 4$	3.9392×10^{-3}	–	3.9623×10^{-3}	–	3.9702×10^{-3}	–
$I = 8$	1.5683×10^{-4}	4.65	1.4841×10^{-4}	4.74	1.3396×10^{-4}	4.89
$I = 16$	5.3627×10^{-6}	4.87	4.8431×10^{-6}	4.94	4.1707×10^{-6}	5.01
$I = 32$	1.6897×10^{-7}	4.98	1.5327×10^{-7}	4.98	1.3293×10^{-7}	4.97
$I = 64$	5.3017×10^{-9}	4.99	4.8092×10^{-9}	4.99	4.1670×10^{-9}	5.00

GMDD
7, 4251–4290, 2014

Table 3. Numerical errors and convergence rates for case 2 with flow in north-east direction ($\gamma = \frac{\pi}{4}$).

Grid	l_1 error	l_1 order	l_2 error	l_2 order	l_∞ error	l_∞ order
G_6	3.394×10^{-5}	–	5.492×10^{-5}	–	1.868×10^{-4}	–
G_{12}	1.440×10^{-6}	4.56	2.321×10^{-6}	4.56	8.924×10^{-6}	4.39
G_{24}	5.367×10^{-8}	4.75	8.317×10^{-8}	4.80	3.457×10^{-7}	4.69
G_{48}	1.942×10^{-9}	4.79	2.957×10^{-9}	4.81	1.487×10^{-8}	4.54

GMDD
7, 4251–4290, 2014

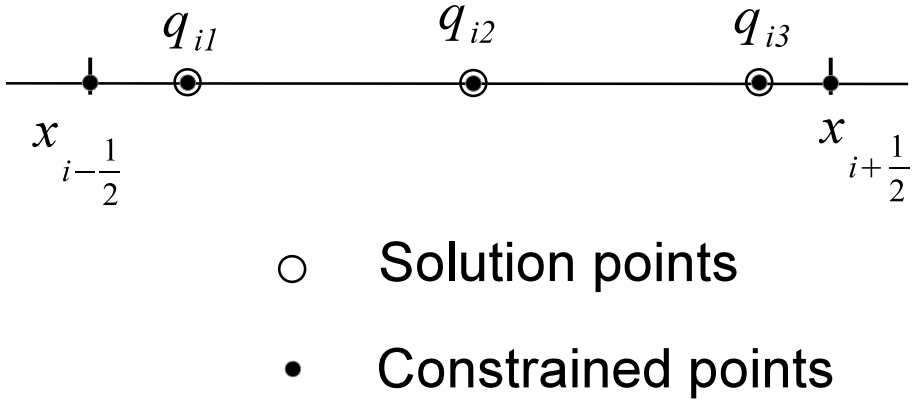

Figure 1. Configuration of DOFs and constrained conditions in one dimensional case.

GMDD
7, 4251–4290, 2014

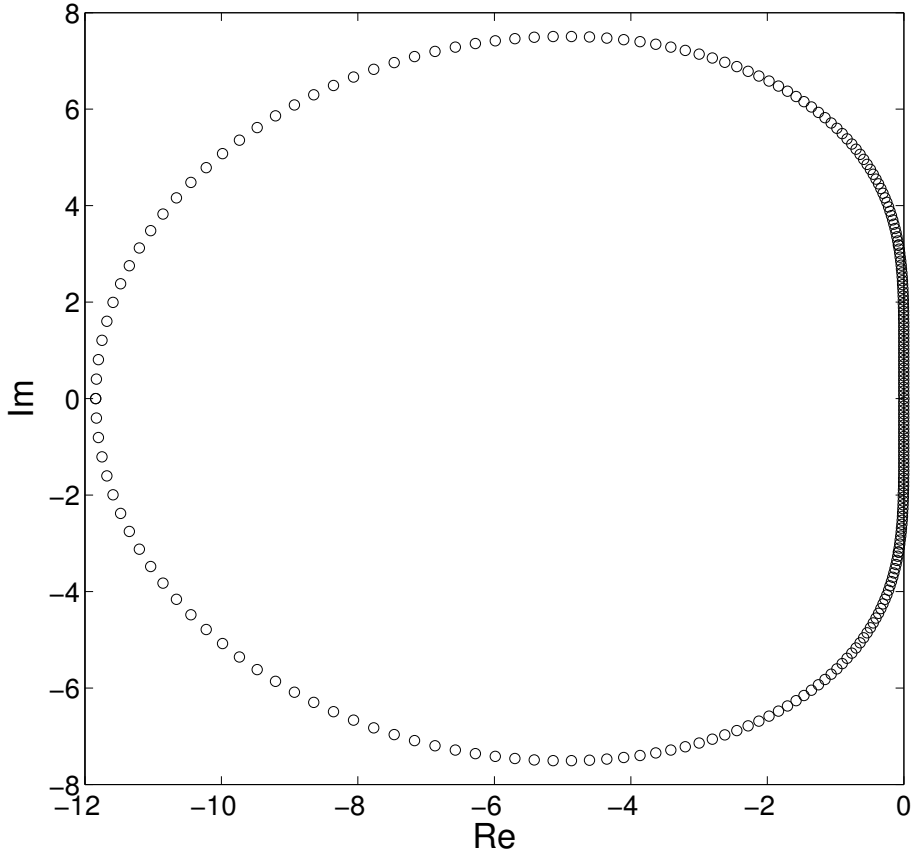

Figure 2. The spectrum of the semi-discrete scheme.

GMDD
7, 4251–4290, 2014

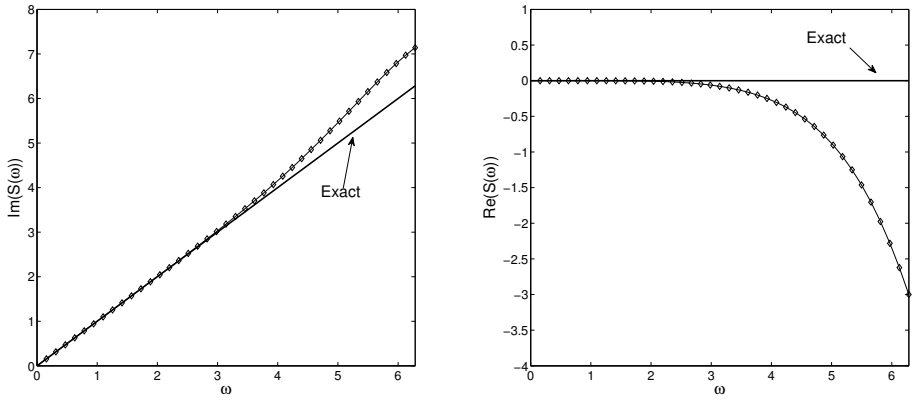

Figure 3. Numerical dispersion (left) and dissipation (right) relations of the semi-discrete scheme.

GMDD
7, 4251–4290, 2014

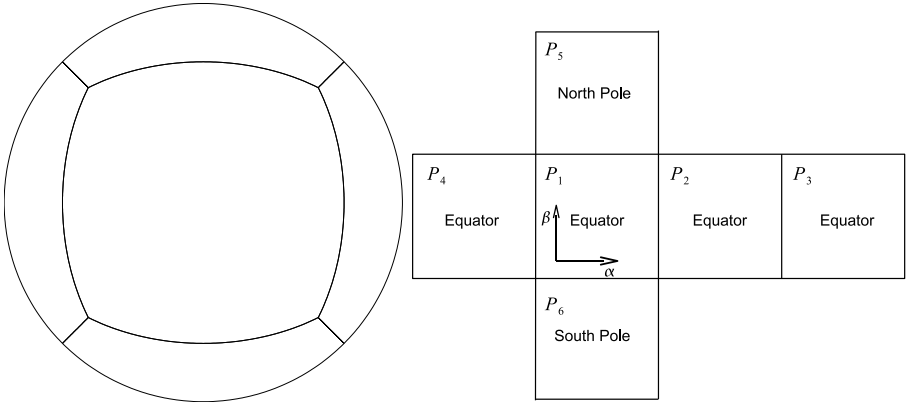

Figure 4. The cubed-sphere grid.

GMDD
7, 4251–4290, 2014

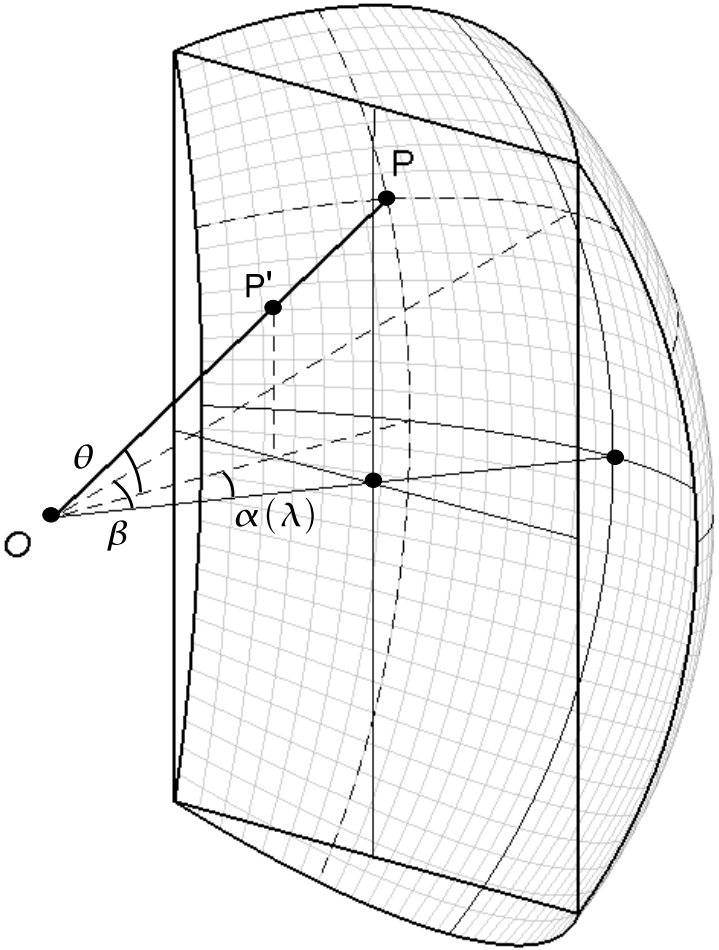

Figure 5. The gnomonic projection.

GMDD
7, 4251–4290, 2014

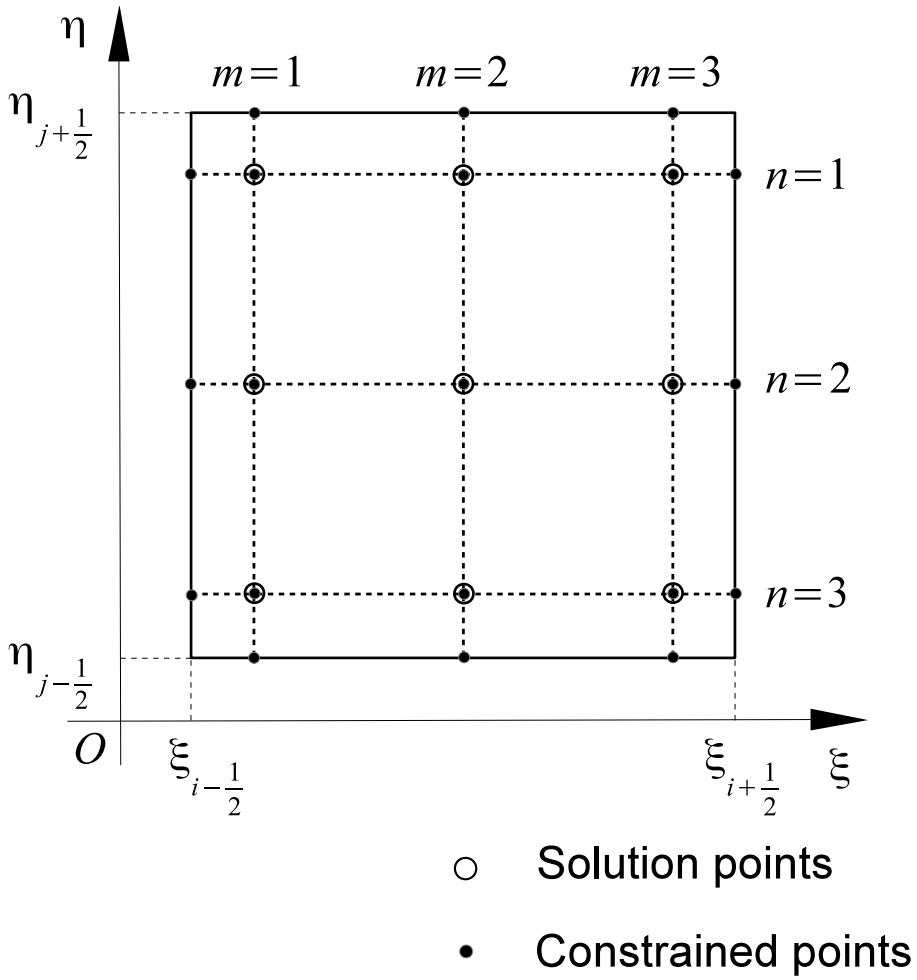

Figure 6. Configuration of DOFs and constrained conditions in two dimensional case.

GMDD
7, 4251–4290, 2014

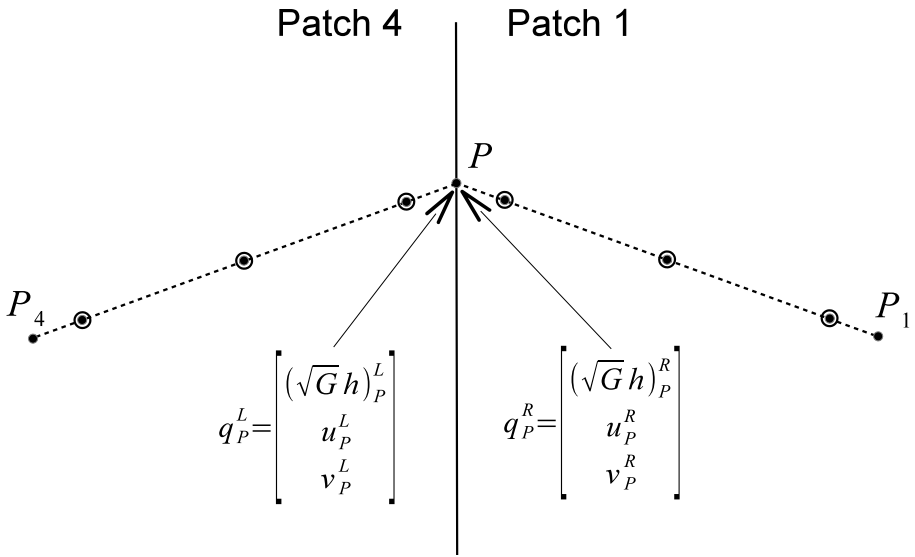

Figure 7. Riemann problem along patch boundary edge between patch 1 and 4.

GMDD
7, 4251–4290, 2014


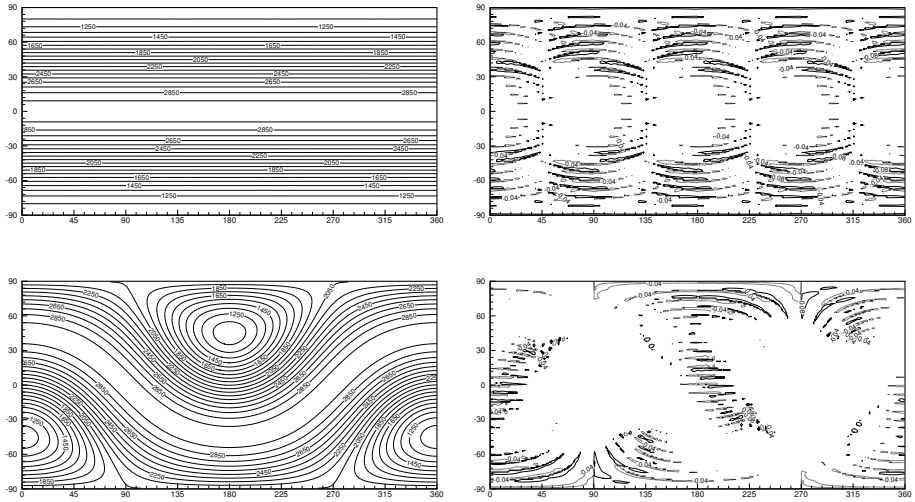

Figure 8. Numerical results and absolute errors of water depth for case 2 on grid G_{12} at day 5. Shown are water depth (top-left) and absolute error (top-right) of the flow with $\gamma = 0$ and water depth (bottom-left) and absolute error (bottom-right) of the flow with $\gamma = \frac{\pi}{4}$.

GMDD
7, 4251–4290, 2014

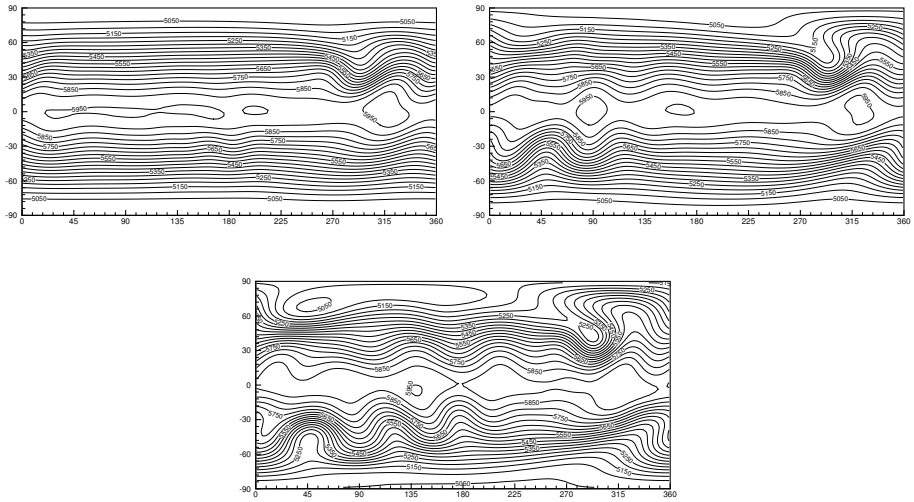

Figure 9. Numerical results of total height field for case 5 on grid G_{12} at day 5 (top-left), day 10 (top-right) and day 15 (bottom).

GMDD
7, 4251–4290, 2014

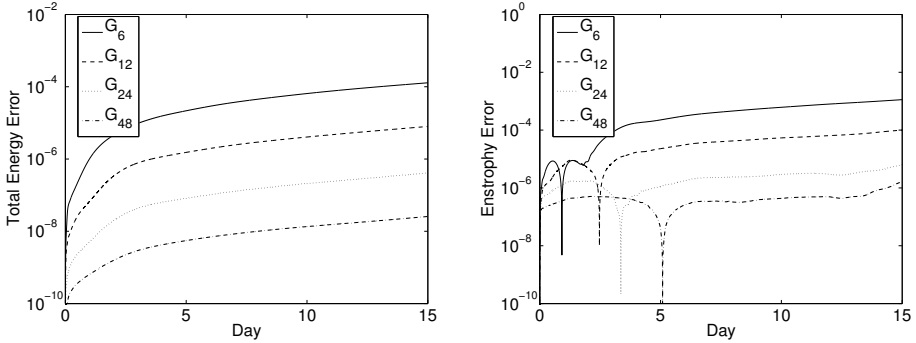

Figure 10. Normalized conservation errors of total energy and potential enstrophy on refined grids for case 5.

GMDD
7, 4251–4290, 2014

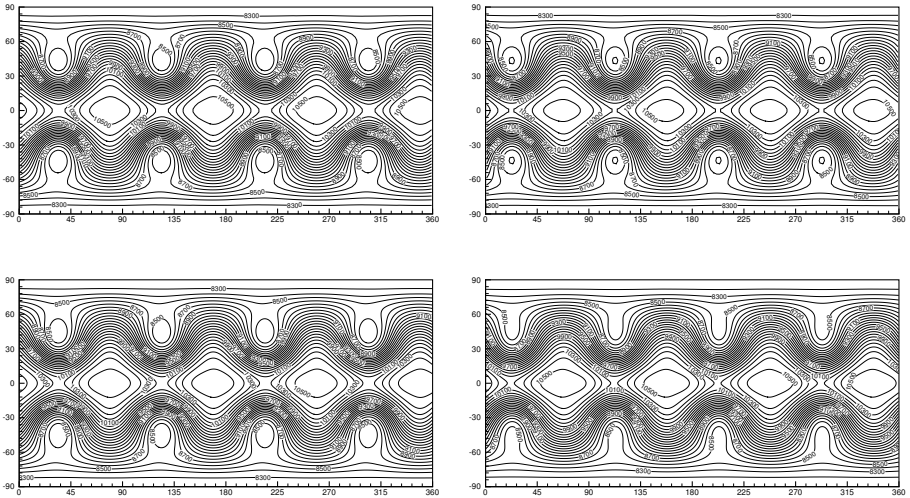

Figure 11. Numerical results of water depth for Rossby–Haurwitz wave test on grid G_{12} at day 7 (top-left), day 14 (top-right) and on grid G_{24} at day 7 (bottom-left) and day 14 (bottom-right).

GMDD
7, 4251–4290, 2014

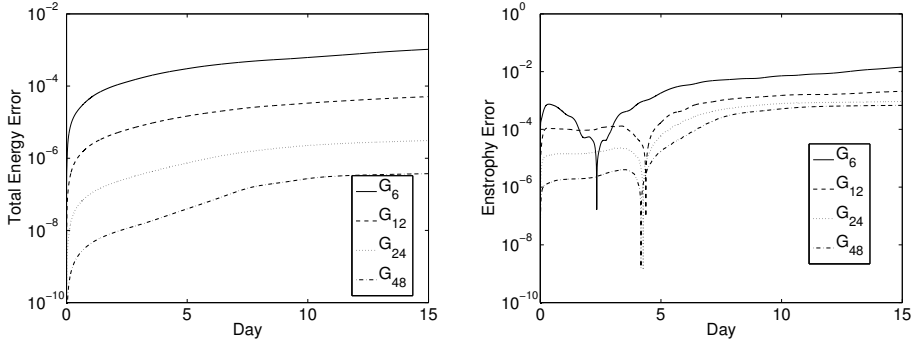

Figure 12. Normalized conservation errors of total energy and potential enstrophy on refined grids for Rossby–Haurwitz wave test.

GMDD
7, 4251–4290, 2014

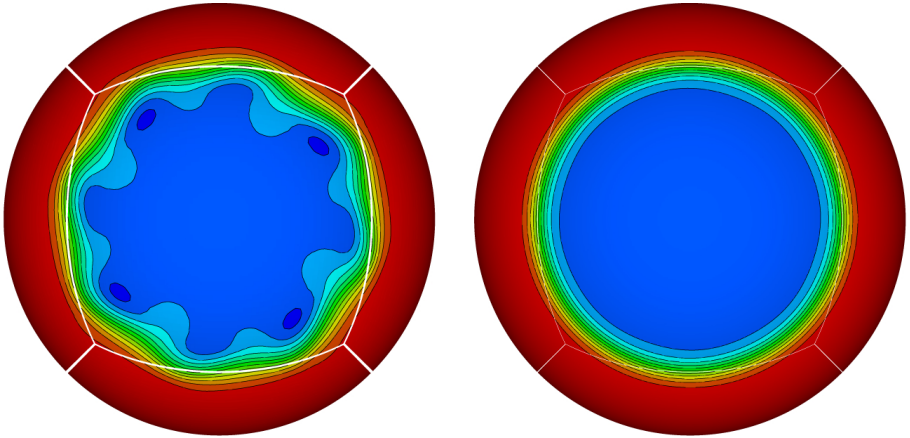

Figure 13. Numerical results of water depth for balanced setup of barotropic instability test on two grids G_{24} (left) and G_{72} (right). Contour lines vary from 9000 m to 10 100 m.

GMDD
7, 4251–4290, 2014

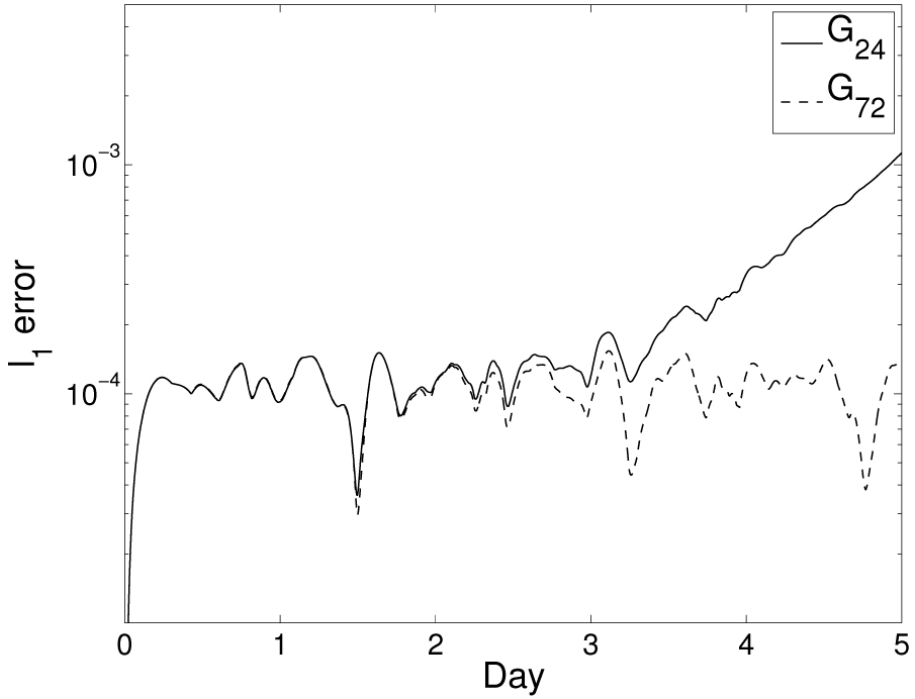

Figure 14. Normalized l_1 error of water depth for balanced setup of barotropic instability test on two grids.

GMDD
7, 4251–4290, 2014

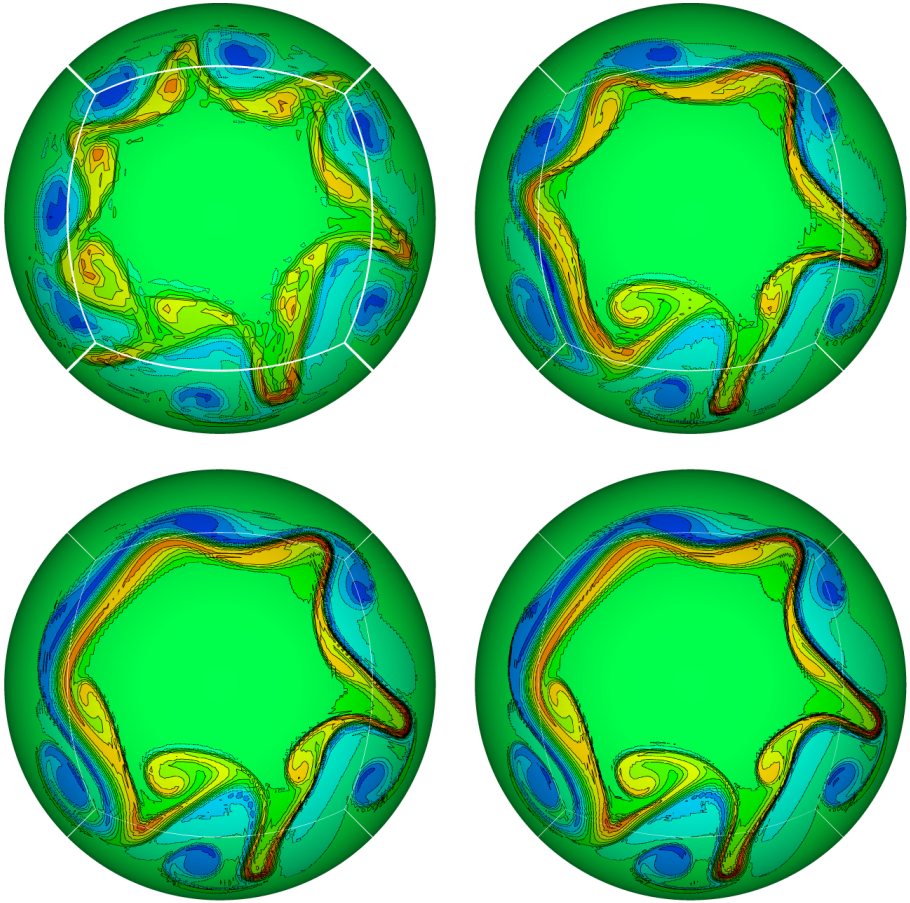

Figure 15. Numerical results of relative vorticity for unbalanced setup of barotropic instability test on a series of refined grids. Contour lines vary from -1.1×10^{-4} to -0.1×10^{-4} by dashed lines and 0.1×10^{-4} to 1.5×10^{-4} by solid lines.

GMDD
7, 4251–4290, 2014